Supplementary material: Colliding respiratory jets as a mechanism of air exchange and pathogen transport during conversations

Arghyanir Giri, Neelakash Biswas, Danielle Chase, Nan Xue, Manouk Abkarian, Simon Mendez, Sandeep Saha, Howard A. Stone

(Received xx; revised xx; accepted xx)

1. Details of numerical simulation

Direct numerical simulations are performed using the open source Fortran 90-95 based solver Xcompact3D (Bartholomew et al. 2020). The governing equations are the incompressible Navier-Stokes equations (1.1 - 1.2) with air as the working fluid,

$$\nabla.\vec{U} = 0, \tag{1.1}$$

$$\frac{D\vec{U}}{Dt} = -\frac{1}{\rho}\nabla P + \nu\nabla^2\vec{U}. \tag{1.2}$$

The kinematic viscosity of air is specified as $1.51\times10^{-5}m^2/s$ corresponding to a constant ambient temperature of $20°C$. The computational domain ($L_x \times L_y \times L_z$) is discretised into a uniform Cartesian mesh of $N_x \times N_y \times N_z$ mesh nodes. The domain size and the number of mesh nodes used are presented in table 1. Boersma et al. (1998) showed that for a round turbulent jet the Kolmogorov length scales were of the order of $0.08D$ (D being the jet diameter) at a streamwise distance $20D$ for $Re = 2.4 \times 10^3$. The grid resolution in the present simulation is $0.08D_{eq}$ (where $D_{eq} \equiv 2\sqrt{ab}$ is the equivalent diameter of the orifice, a and b being the semi-major and semi-minor axes of the mouth respectively, $a = 1.5$ cm and $b = 1$ cm) at a lower average Re compared to Boersma et al. (1998) and hence all scales of dynamical importance are expected to be resolved. The velocity is set to zero in the whole computational domain at $t = 0$.

Fig. 1 shows a central slice of the 3-dimensional domain of the simulation along with the boundary conditions. An outflow boundary condition is also applied to the lateral surfaces normal to the slice. A top hat velocity profile is applied at both the inlets as given in equation 1.3:

$$V(x,y) = \frac{V_{cl}}{2}\left[1 + tanh\left(\frac{D_{eq}}{\theta}\frac{1-(\frac{x}{a})^2-(\frac{y}{b})^2}{\sqrt{(\frac{x}{a})^2+(\frac{y}{b})^2}}\right)\right] \tag{1.3}$$

Here V_{cl} is the centerline velocity, which is adjusted to yield the target flow rate displayed in the main text (Fig.1b). Here θ is the momentum thickness of the jet. No external disturbances were applied on top of the velocity signals used in the simulations. The first- and second-order spatial derivatives were discretised using a 6th-order compact scheme and the 3rd-order Adams-Bashforth scheme was used for time integration. The time step used was $10^{-4}s$, which was small enough to ensure that the CFL number was kept low. The divergence-free condition is ensured up to the machine accuracy using the

L_x(m)	L_y(m)	L_z(m)	N_x	N_y	N_z
1	0.8	0.8	501	401	401
1.5	1.25	1.25	751	627	627

TABLE 1. Parameters for the numerical simulations.

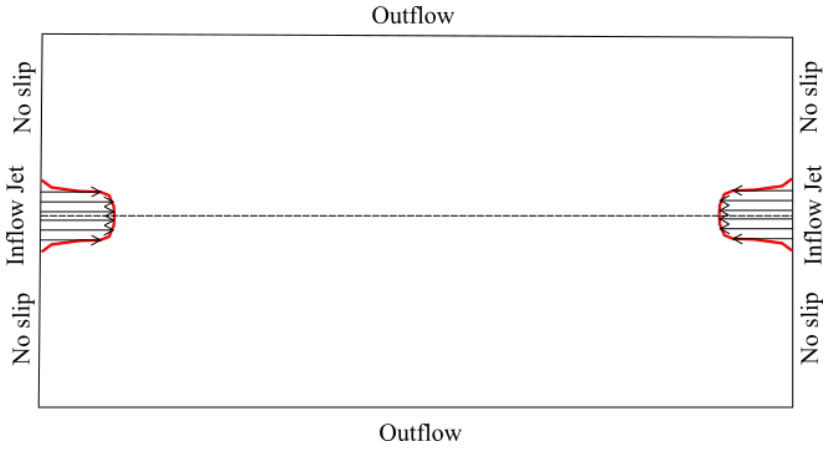

FIGURE 1. Boundary conditions used in numerical simulations

concept of modified wavenumber (Laizet and Lamballais 2009). The mesh for pressure distribution is staggered from the velocity mesh to avoid spurious pressure oscillations (see Laizet and Lamballais (2009) for more details).

Tracer particles are injected from the orifice at an uniform rate at an interval of 0.01 seconds. The particles are randomly distributed inside the orifice area. We solve for the trajectory of the particles, $\vec{X}$, using the equation for the pathline (Eq. 1.4),

$$\frac{d\vec{X}}{dt} = \vec{U}. \tag{1.4}$$

The time integration of the Eq. 1.4 is carried out numerically using the modified Euler method (for details of the algorithm see Pozrikidis (2009, pp 23)).

Our DNS results are validated against the large eddy simulation (LES) data from Abkarian et al. (2020) for a single jet case $S50$ (see Abkarian et al. (2020) for details) in Fig. 2. A good agreement is observed between the length of the jets (obtained based on 90% of the total number of particles residing within that length similar to Abkarian et al. (2020)) and the results are insensitive to inflow disturbances.

2. Details of flow visualization experiments

Experiments were conducted using a scaled model of the simulations as shown in Fig. 3. The axial distance between the orifices is $L = 25$ cm. Experiments for four transverse offset distances were performed: $d = 0,\ 0.625,\ 1.25$, and 2.5 cm. A reservoir (a glass container with the volume of one liter) supplies pressurized air to 1/4" tubing. The tubing

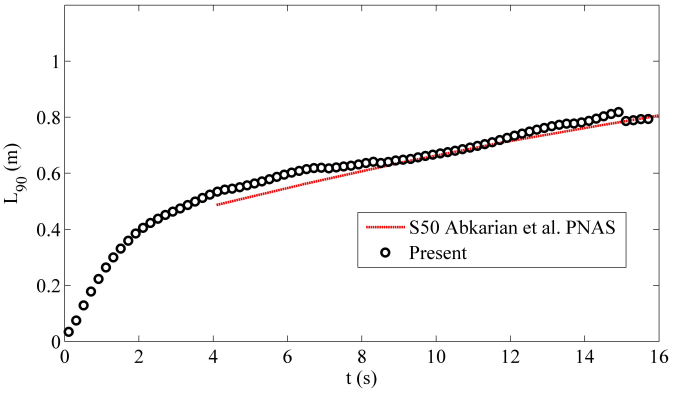

FIGURE 2. Validation of numerical simulations.

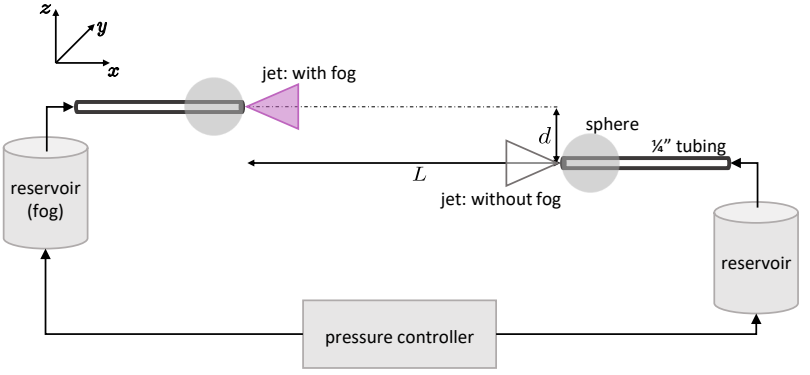

FIGURE 3. Experimental setup. Two spheres are placed an axial distance L apart with a transverse offset d. A reservoir supplies pressurized air, set by a pressure controller, to the tubing which goes through the hollow sphere. One reservoir is seeded with fog for visualization of the jet using a laser sheet in the xz plane.

is connected from the reservoir through a hollow sphere with a 1.4 in diameter, and the outlet of the tubing is at the surface of the sphere. The pressurized air exiting the orifice creates a jet, Re = 700. The pressurized air is controlled by a pressure pump (Elveflow), and the flow rate is calibrated by a flowmeter (Bourrianne et al. 2020). One reservoir is seeded with fog (generated with a fog machine by American DJ using the fog juice by Froggys Fog) to visualize the jet in the xz plane. A laser sheet (wavelength $\lambda = 532$ nm) illuminates the center plane of the jet ($y = 0$). A high-speed camera (Phantom v7.3) perpendicular to the laser sheet captures images of the jet at a frame rate of 200 fps. To extract the contour of the injected fog in the experiments, we set a threshold for the image according to Otsu's method (Otsu 1979); see the typical extracted shapes of the injected fog in Figs 3(A-D) of the manuscript and Supplementary Movies 1-4. Note that the concentration of the fog in the reservoir decreases when the air is pressurized, and the fading of the intensity of the fog in the experiments is complemented in the image processing.

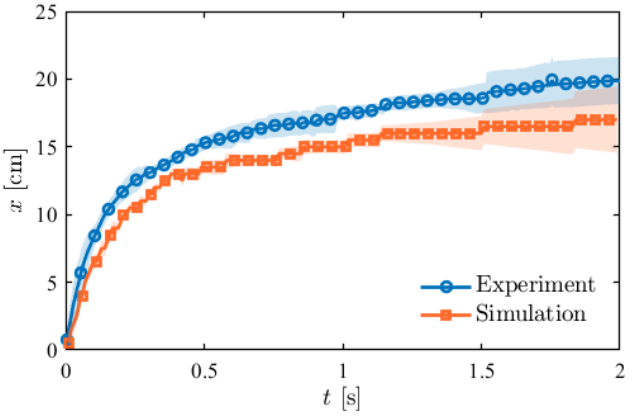

FIGURE 4. Comparing the jet propagation in the x-direction from the experiments (indicated with blue) and the simulations (indicated with orange) at non dimensional offset height $d_n = 0$. The distance $L = 0.25$m with Re 700 is same for both the experiments and the simulations. The orifice for the jets in the simulations were circular and of the same radius like in the experiments.

3. Validating numerical simulations against experiments

The distance L in the simulations, is the typical distance between two people when conversing face to face following social distancing norms. The dimensions in the experiments have been scaled down by 4 times including L, keeping the Reynolds number same, because of physical constraints in the experimental setup. We have run the simulation for steady jets with the same scaled down L, as in the experiments. Also, we have matched the Re approximately and the orifice radius is identical for both. Figure 4 compares the axial spreading of the jets from the experiments and the simulations at $d_n = 0$. It is apparent that the jet extent plots follow a similar trend qualitatively. The random disturbances inherently present could explain the minor deviation observed in the simulation and experimental data.

4. Analysis of offset angle

In a real life scenario the taller speaker might instinctively look down and the shorter might tend to look up. However, the present work studies only a simplified version of the real-life problem consisting of additional complexities to gain insight. The importance of the angle between the jets was considered initially but the evidence in the literature Tang et al. (2011) indicates that the offset angle. θ, itself could be small over certain intervals. Our analysis reveals that the angle of the jet centerlines with respect to the horizontal (offset angle, $\theta \equiv \beta - \delta$ where δ, β are defined as the angle between the horizontal and the bisector of the angle subtended at the lips of Speakers 1,2 respectively at every instant as seen in Fig. 5(A) below) is not always significant; hence justifying the assumption that the offset angle is negligible in our model. A frame by frame image processing of a video of two subjects talking face to face Tang et al. (2011) was carried out to find the offset angle, θ. Figure 5(B) below shows that the instantaneous offset angle does not exceed 1° and the mean offset angle over the interval is found to be around 0.17° which is very small while the offset height varies between $2 - 8$ cm and is hence non-negligible. This is indicative of the fact that during a conversation, two people naturally minimise the offset angle without compensating for the offset height.

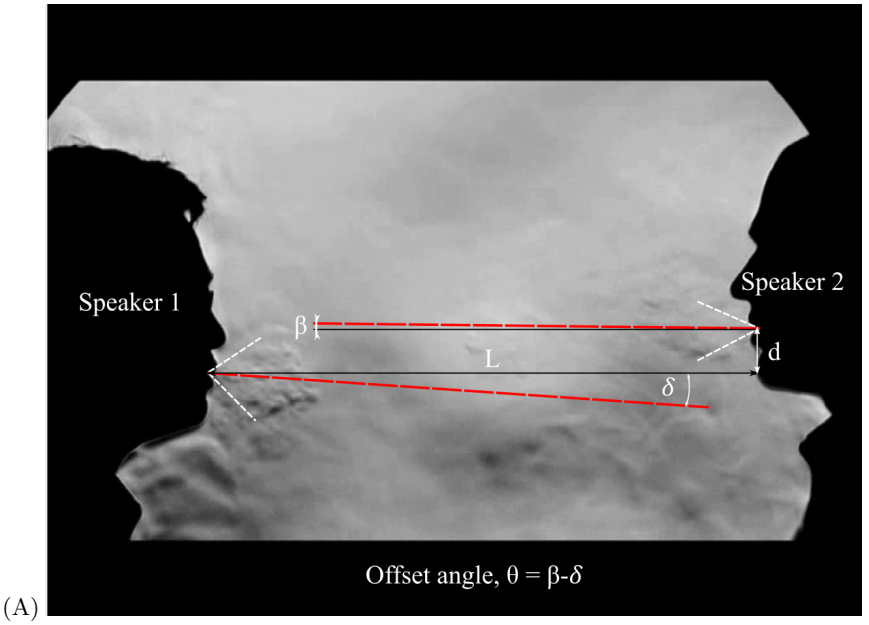

(A)

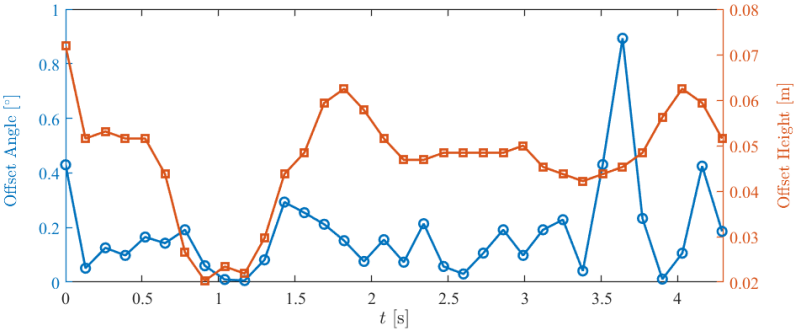

(B)

FIGURE 5. (A) Two people facing each other during a conversation (movie S4 of Tang *et. al.* Tang et al. (2011)). The offset angle, θ is defined as $\beta - \delta$, where δ, β are the angles between the jet centerlines and the horizontal of speaker 1 and 2 respectively. The jet centerline is approximated as the bisector of the angle subtended at the lips. (B) The time dependence of offset angle (indicated with blue) and offset height, d, (indicated with orange) during a conversation.

5. **Statistical convergence**

The major uncertainty in the jet propagation arises due to turbulence. We use approximately $\sim 1.1 \times 10^5$ particles per breath (of 4 seconds), so we expect the results to be statistically converged. However, we have investigated the quantitative effects as well, by adding random disturbances at the inlet for $d_n = 0.83$. A comparison of the streamwise length L_{90} for this case is presented with and without disturbances in Figure 6 here. The axial spreading plots for both the cases follow very similar trends without any significant deviations.

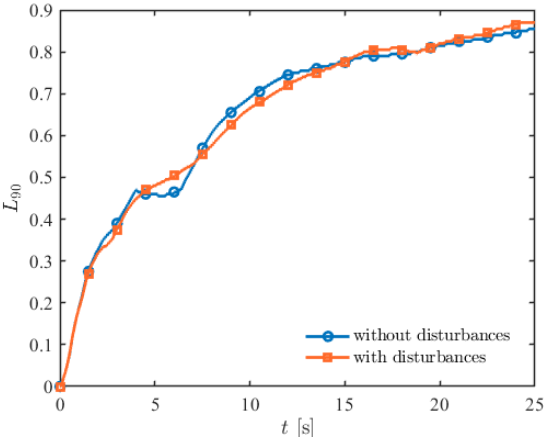

FIGURE 6. The time dependence of streamwise length L_{90} for non-dimensional offset $d_n = 0.83$, solid blue line with circular marker denotes the axial spreading without disturbances and the solid orange line with square markers represent the axial spreading with disturbances.

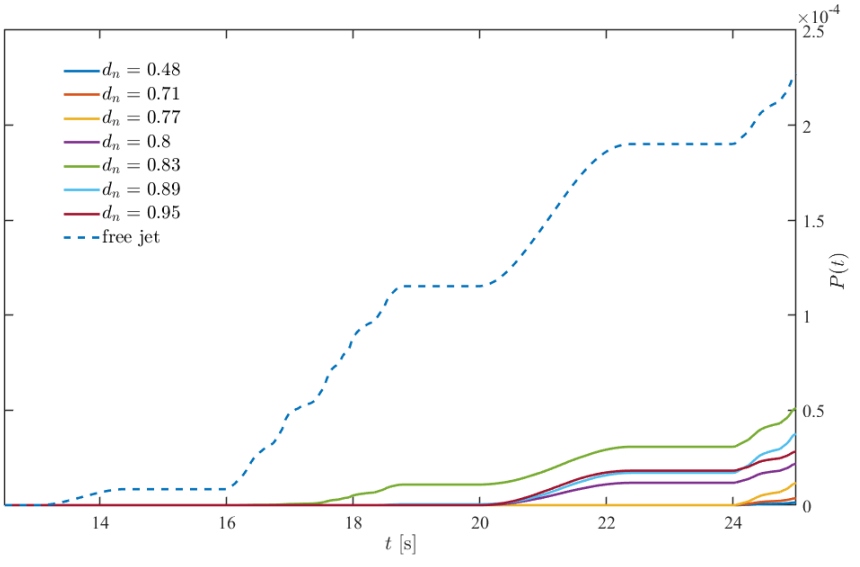

FIGURE 7. The variation of infection probability $P(t)$ with speaking time t

6. **Infection risk probability plot**

We used a semi-log plot to highlight the variation in the order of magnitude of infection probability $P(t)$ for a separation distance of 1 m. between different cases as in a linear plot the difference between the cases are not properly visible as can be seen in Figure 7.

REFERENCES

M. Abkarian, S. Mendez, N. Xue, F. Yang, and H. A. Stone. Speech can produce jet-like transport relevant to asymptomatic spreading of virus. *Proceedings of the National Academy of Sciences*, 117(41):25237–25245, 2020.

P. Bartholomew, G. Deskos, R. A. Frantz, F. N. Schuch, E. Lamballais, and S. Laizet. Xcompact3d: An open-source framework for solving turbulence problems on a cartesian mesh. *SoftwareX*, 12:100550, 2020.

B. J. Boersma, G. Brethouwer, and F. T. Nieuwstadt. A numerical investigation on the effect of the inflow conditions on the self-similar region of a round jet. *Physics of Fluids*, 10(4): 899–909, 1998.

P. Bourrianne, S. Chidzik, D. Cohen, P. Elmer, T. Hallowell, T. J. Kilbaugh, D. Lange, A. M. Leifer, D. R. Marlow, P. D. Meyers, et al. Inexpensive multi-patient respiratory monitoring system for helmet ventilation during COVID-19 pandemic. *medRxiv*, 2020.

S. Laizet and E. Lamballais. High-order compact schemes for incompressible flows: A simple and efficient method with quasi-spectral accuracy. *Journal of Computational Physics*, 228 (16):5989–6015, 2009.

N. Otsu. A threshold selection method from gray-level histograms. *IEEE transactions on systems, man, and cybernetics*, 9(1):62–66, 1979.

C. Pozrikidis. *Fluid dynamics: theory, computation, and numerical simulation*. Springer, second edition, 2009.

J. W. Tang, A. D. Nicolle, J. Pantelic, M. Jiang, C. Sekhr, D. K. Cheong, and K. W. Tham. Qualitative real-time schlieren and shadowgraph imaging of human exhaled airflows: an aid to aerosol infection control. *PLoS One*, 6(6):e21392, 2011. © 2011 Tang et al. This is an open-access article distributed under the terms of the Creative Commons Attribution License, which permits unrestricted use, distribution, and reproduction in any medium, provided the original author and source are credited.